# Aggregation-Induced Asymmetric Charge States of Amino Acids in Supramolecular Nanofibers

Li, Y<sup>a, b</sup>; Kim, M<sup>c</sup>; Pial, T.H. b, d; Lin, Y<sup>b, g</sup>; Cui, H<sup>c, e</sup>; Olvera de la Cruz, M<sup>a, b, d, f, g\*</sup>

<sup>a</sup>Department of Chemical and Biomolecular Engineering, Northwestern University, 2145 Sheridan Road, Evanston, IL 60208, United States

<sup>b</sup>Center of Computation and Theory of Soft Materials, Northwestern University, 2145 Sheridan Road, Evanston, IL 60208, United States

<sup>c</sup>Department of Chemical and Biomolecular Engineering and Institute for NanoBiotechnology, Johns Hopkins University, 3400 North Charles Street, Baltimore, MD 21218, United States

<sup>d</sup>Department of Materials Science and Engineering, Northwestern University, 2220 Campus Drive, Evanston, IL 60208, United States

<sup>e</sup>Department of Oncology and Sidney Kimmel Comprehensive Cancer Center, Johns Hopkins University School of Medicine, Baltimore, MD 21205, United States

Department of Physics and Astronomy, Northwestern University, 2145 Sheridan Road, Evanston, IL 60208, United States

Department of Chemistry, Northwestern University, 2145 Sheridan Road, Evanston, IL 60208, United States

\* Email: m-olvera@northwestern.edu

KEYWORDS: peptide amphiphile, supramolecular assembly, charge regulation, acidbase equilibrium, molecular dynamics **ABSTRACT**: Electrostatic interactions contribute critically to the kinetic pathways and thermodynamic outcomes of peptide self-assembly involving one or more than one charged amino acids. While it is well understood in protein folding that those amino acids with acidic/basic side chains could shift their pKas when placed in a hydrophobic microenvironment, it remains unclear to what extent aggregation of monomeric peptide units from the bulk solution could alter their charged status and how this change in pKa values would reciprocally impact their assembly outcomes. Here, we design and analyze two solution systems containing peptide amphiphiles with hydrocarbon chains of different lengths to determine the factor of deprotonation on assembly. Our results suggest that models of supramolecular nanofibers with uniformly distributed, fully charged amino acids are oversimplified. We demonstrate, with molecular dynamics simulations and validate with experimental results that asymmetric, different protonation states of the peptides lead to distinct nanostructures after self-assembly. The results give estimates on the electrostatic interactions in peptide amphiphiles required for their self-assembly and shed light on modeling molecular assembly systems containing charged amino acids.

## Introduction

Peptide amphiphile (PA) self-assembly has been extensively studied over the past decades¹. Peptide amphiphiles designed with different hydrophobic tails and peptide heads self-assemble into various structures²,³, achieving functions such as mineralization⁴,⁵, cell proliferation⁶,७, molecular imaging³-¹⁰, drug delivery¹¹-¹³, and pH sensing¹⁴. Moreover, the self-assembly of PA is essential in immunology studies¹⁵-¹⁰, where PA materials have shown superior advantages. Research demonstrates that carefully designed PA superstructures can lead to strong bindings with certain enzymes¹⁵-¹¹. Barrett *et al* discovered that PA micelles induce stronger immunological response¹¹. Li *et al* showed PA fibers can reversely bind with antibodies¹³,¹¹⁰. To achieve controlled assembly for desired structures, understanding the relevant interactions is vital²⁰.

Electrostatic interactions contribute to a large number of systems including patterns on polyelectrolyte brushes<sup>21,22</sup>, nanoparticles functionalized with ligands with end charged groups forming gels<sup>23,24</sup> or crystals<sup>25</sup> besides PA micelles and fibers<sup>26,27</sup>. The charges in PA are usually carried by the sidechains of amino acids. Given their weak acid/base nature, charge regulation of amino acids varies due to numerous factors, such as pH, molecule concentration, and microenvironment. Research unveils that the charge states of amino acids shift by an unexpected amount under different conditions<sup>28–30</sup>. Isom *et al* showed that, in a single protein, depending on the microenvironment, glutamic acid (GLU) has a pKa ranging from 4.5 - 9.5 with a theoretical value of 4.5<sup>28</sup>. Similarly, the self-assembly process of PA brings changes in the chemical environment of the assembled molecules. The pKa shift of amino acids in peptide amphiphiles upon self-assembly has been long noticed in experiments<sup>29,30</sup>.

Theorists have made efforts to predict the acid-base equilibrium between the protonated and deprotonated acids in PA self-assembly under different pH and salt conditions  $^{31,32,33}$ . However, the phenomenon draw few attention in simulation works  $^{34,35}$ . All amino acids are usually assumed to be charged if they have acidic/basic side chain.

The first reason is the computation expense in molecular dynamics (MD) simulations. Even though many successful attempts have been made using the continuum model $^{21,36}$ , simulating pH effects in the atomistic scale is still challenging and expensive. Furthermore, the time scale that atomistic simulations can reach is limited. It is hard to capture structural transitions in complex PA systems. Therefore, in these cases, regardless of the strong approximations, fully charged PA models often yield qualitative accurate results $^{32}$ . Another major reason lies in the deceiving fact that amino acids are calculated to be charged using experimental pH and the theoretical pKas of the amino acids. However, the pKa of an amino acid is a function of its surroundings $^{37}$  and can vary significantly. Shifts in the pKas of amino acids are often underestimated.

In this paper, we demonstrate that microenvironments have decisive effects on the charge states of amino acids and the resulting quantitative difference in the charge would lead to a qualitative change in the nanostructure of PA assembly. The charge states of the fiber should be discreetly described to accurately depict the properties of the fiber. As shown here, overestimating electrostatics in the PA superstructures yields significant deviations in various physical properties including their structural density, charge density, and the degree of salt ion condensation. Furthermore, on the macroscale, PA fiber interactions that depend on the surface charges would be modified.

Motivated by the immunology studies on short carbon PAs, we first focus on a specific system of nanofiber self-assembled by hydrophobic-hydrophilic patterned peptide amphiphiles with a short hydrophobic segment. This system is especially amenable to determine the competition between hydrophobic and electrostatic interactions in PAs self-assembly into either spherical micelles or cylindrical fibers. In contrast, in systems with large carbon chains, the hydrophobic interactions usually dominate, and fibers are formed regardless of the charge states of the amino acids in MD simulations where the amino acids are generally assumed to be fully charged. The chemical structure of the molecule in this study is shown in *Fig. 1a*. In the system, 2 kinds of acid-base equilibrium exist:

$$C_{12} - VVE_1^0E_2 \rightleftharpoons C_{12} - VVE_1^{-1}E_2 + H^+$$
(1)

$$C_{12} - VVE_1E_2^0 \rightleftharpoons C_{12} - VVE_1E_2^{-1} + H^+$$
(2)

The superscript denotes the charge states of the Glutamic acid (referred to as GLU or E), where  $\bf 0$  means the protonated state where the residue is not charged and  $\bf -1$  means the deprotonated state where the residue carries a negative charge. The subscript denotes the location of GLU in the sequence. Experimentally, the PAs form nanofibers under  $pH = 7.3 \sim 7.4^{18}$ . Usually, both GLUs are assumed to carry a negative charge under the experimental pH condition due to the very low pKa of GLU in bulk solutions. However, we hypothesize that the self-assembly process would create different microenvironments for GLUs: the inner GLU (E<sub>1</sub>) will locate around the boundary between the hydrophobic cores and the solvent. With limited access to polar solvents and ions, the protonation states are expected to be different from the bulk condition. Furthermore, in the case of short peptide

amphiphile systems, the repulsive interactions between charged amino acids become significant. Therefore, a discrepancy between the fully charged PA assumption in simulations and experimental results is expected. Here, C<sub>16</sub>-VVEE fibers systems are also studied to demonstrate that MD simulations give qualitatively similar results regarding fiber formation regardless of the assumptions in the charge states of the amino acids when hydrophobic interactions dominate yet structural properties such as amino acid packing and ionic cloud distributions in the fibers are affected.

In the following sections, results from atomistic and coarse-grained simulations are shown to validate the hypothesis. Different charge conditions in the formation of cylindrical fibers and spherical micelles are discussed. Titration experiments and analytical fittings are carried out to further support the assumptions.

## **Methods**

#### **Atomistic simulations**

GROMACS 2021.5<sup>38</sup> is used to perform molecular dynamics (MD) simulation in this paper. GROMACS is an MD package mainly designed for simulations of large biomolecules. The CHARMM36<sup>39</sup> force field is used for all-atom simulations. The CHARMM TIP3P combined with the SETTLE algorithm<sup>40</sup> is used to model water molecules. All visual analyses are performed with VMD<sup>41</sup> and MDAnalysis<sup>42</sup>.

The PA molecule is initialized with Avogadro<sup>43</sup> and Packmol<sup>44</sup>. On the xy-plane, 9 PAs are distributed radially with an angle of  $40^{\circ}$  between each other to form the first layer. The second layer of 9 PAs is placed 0.5 nm above the first layer with a  $20^{\circ}$  shift. A total of 16 layers are created to initialize the fiber<sup>45</sup>. The fiber is solvated in water with 0.1 M of NaCl except for the counterions. The initial structure is shown in *Fig. 1*. The system is equilibrated with gradually decreasing force constants applied on the  $C_{12}$ . A subsequent production run is performed on the fully relaxed system for 200 ns. All detailed parameters for the simulation can be found in the *Supplementary Information* (SI). The final simulation snapshots are shown in *Fig. 2*. Same procedures are performed for  $C_{16}$ -VVEE PA systems.

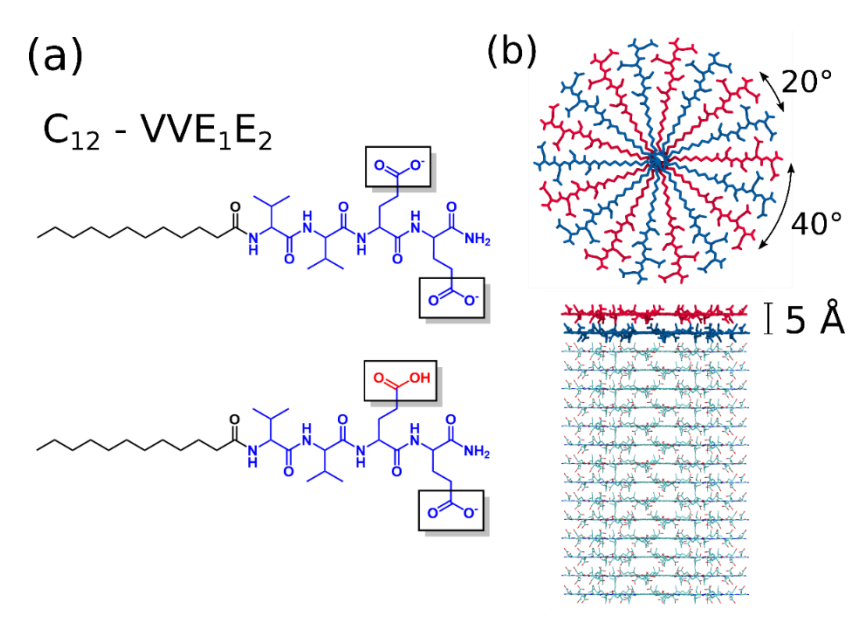


**Figure 1.** Chemical structures of the studied peptide amphiphiles and schematic illustration of the initial setup for atomistic simulations. (a) The peptide amphiphile molecule for the fiber simulation. The first molecule is fully deprotonated and carries **-2e** charges. The second molecule is half protonated and carries **-1e** charges. (b) The initial structure of the fiber.

## Coarse-grained simulation

GROMACS 2021.5 and MARTINI 3 force field<sup>46</sup> are combined in the coarse-grained simulations. The details of the PA bead mapping are provided in *Fig.* **S3** in SI. We solvate 150 PAs in an aqueous solution at 0.1M NaCl salt concentration along with counterions in a  $9 \times 9 \times 9$  nm<sup>3</sup> box. Energy minimization is first performed on the system, followed by equilibration under NVT (constant number of molecules, constant volume, and constant temperature) ensemble and then NPT (constant number of molecules, constant pressure, and constant temperature) ensemble. A subsequent production run is performed for 1 µs. Detailed parameters for the simulations are listed in the SI.

#### Local Debye length

The original formula for Debye length calculation is

$$\lambda_D = \sqrt{\frac{\varepsilon_r \varepsilon_0 k_B T}{\sum (Z_i e)^2 C_i}}$$
(3)

The Debye length depends on the ion concentrations and the relative permittivity. In the specific system, Na<sup>+</sup> tends to concentrate around the fiber to neutralize the negative charges carried by the PA molecules. The dielectric constant is assumed to be proportional to the volume fraction of oil ( $\varepsilon_r=2$ ) and water ( $\varepsilon_r=80$ ). Therefore, the Debye length varies depending on the radial distance from the fiber center.

$$\lambda_D(r) = \sqrt{\frac{\varepsilon_r(r)\varepsilon_0 k_B T}{\sum (Z_i e)^2 C_i(r)}}$$
(4)

The local ion concentration can be calculated based on the simulation results with the radial distribution function (RDF):

$$C(r) = \frac{dN}{dV} = g(r) \times \rho_0 \tag{5}$$

With a 2D radial distribution,  $dV = 4\pi r dr$ .

Therefore, the local Debye length is

$$\lambda_D(r) = \sqrt{\frac{4\pi r dr \times \varepsilon_r(r)\varepsilon_0 k_B T}{\sum (Z_i e)^2 dN_i}}$$
(6)

#### Titration on PA solutions

First, the PA solutions are prepared. The lyophilized peptide amphiphile powders are first pretreated with 400  $\mu$ L hexafluoro-2-propanol (HFIP) to eliminate any pre-existing structures before assembly. After evaporating off the HFIP under compressed air for a minimum of 20 minutes until a dry thin film formed at the bottom of the tube, enough Nanopure water is added to reach a final concentration of 2.5 mM. The peptide amphiphile solutions were sonicated in a 45°C water bath for 40 minutes before being left overnight in a closed eppendorf tube at room temperature to allow for complete assembly, and the pH was measured before and after the overnight assembly. The preparation of the fibers was done following the protocal described in references 19 and 20. Titration curves are determined by adding 10  $\mu$ L of 0.1M NaOH or HCl at a time to 5 mL of the peptide amphiphile solutions. After each addition of NaOH or HCl, the pH is measured, which is calibrated prior to experiments using pH 4, 7, and 10 buffers.

#### Fitting of the titration curve

The  $C_{12}$ -VVEE molecule is denoted as  $H_2A$  for simplicity. The acid-base equilibrium is considered with the following equations:

$$H_2A + H_2O \rightleftharpoons H_3A^+ + OH^- \qquad K_b$$

$$(7)$$

$$H_2A \rightleftharpoons HA^- + H^+ \qquad K_{a_1}$$

$$(8)$$

$$HA^- \rightleftharpoons A^{2-} + H^+ \qquad K_{a_2} \tag{9}$$

With species conservation and charge neutrality, two final expressions are reached:

$$w + [H^{+}] + \frac{c_{B}V_{B}}{V_{B} + V_{0}} = \frac{K_{w}}{[H^{+}]} + \frac{wK_{w}K_{a_{1}}}{[H^{+}]^{2}K_{b}} + 2\frac{wK_{w}K_{a_{1}}K_{a_{2}}}{[H^{+}]^{3}K_{b}}$$

$$(10)$$

$$w + \frac{wK_{w}}{[H^{+}]K_{b}} + \frac{wK_{w}K_{a_{1}}}{[H^{+}]^{2}K_{b}} + \frac{wK_{w}K_{a_{1}}K_{a_{2}}}{[H^{+}]^{3}K_{b}} = \frac{c_{0}V_{0}}{V_{B} + V_{A}}$$

$$(11)$$

Where w is the concentration of  $H_3A^+$ ;  $K_w$  is the water dissociation constant;  $V_B$  is the volume of NaOH/HCl added;  $V_0$  and  $c_0$  are the initial volume and concentration of the  $H_2A$  solution. The two equations allow extrapolation of the titration curve with the volume of NaOH/HCl added. More details can be found in the SI.

## Results and discussion

Based on both previous experiments and theoretical results, the pKa values of GLUs vary depending on the local environments<sup>28,29</sup>. Under a certain range of pH, it is possible that due to the difference in the microenvironment,  $E_1$  is protonated and carries no charges while  $E_2$  is deprotonated and has a -1e charge in the  $C_{12}$ -VV $E_1E_2$  molecule. We expect that, in these cases, distinct structures would form, and MD simulations can capture the transitions between structures since the hydrophobic interactions do not dominate over the Coulombic repulsions.

Two parallel simulations are performed with the same conditions except for the protonation states of the PA molecules. The atomistic simulation of the half-protonated PA system yields a stable, compactly packed fiber structure ( $Fig.\ 2a$ ), which aligns with experimentally observed structures in literature. The convergence of energy and box size in the z direction indicate the equilibrium is reached ( $Fig.\ S2$  in the SI). Around 9.8% of peptide heads form  $\beta$ -sheets, which help stabilize the structure. The  $C_{12}$  heads form a hydrophobic domain where no water molecules or ions penetrate. In comparison, the fiber composed of fully charged PA molecules breaks down into spherical micelles (hereafter referred to as micelles) ( $Fig.\ 2b$ ). Two micelles have 63 PA molecules and 81 PA molecules respectively.

The change in the equilibrium structure can be attributed to the different protonation states of  $E_1$  and  $E_2$ .  $E_1$  is assumed to be protonated due to (1) decreased relative permittivity, and (2) limited access to ions. The radial distribution functions (RDF) of  $E_1$  and  $E_2$  are shown in **Fig. 2c**. At the ion concentration applied in this study (0.1 M), the Debye length agrees well with experimental measurements and is used to estimate

the interactions between charges<sup>47</sup>. We assume the relative permittivity of the hydrophobic domain is  $\varepsilon_r = 2$  (oil) and the local Debye length  $\varepsilon_r(r)$  is a linear combination of the volume fraction of fiber ( $\varepsilon_r = 2$ ) and water ( $\varepsilon_r = 80$ ). With **Eq (6)**, the Debye length  $\lambda_D(r)$  is calculated (**Fig. 2c**). The local Debye length is ~26.7% larger at the position of E<sub>1</sub> ( $\lambda_1 = 0.76 \ nm$ ) than at the position of E<sub>2</sub> ( $\lambda_2 = 0.60 \ nm$ ). The screening effect is much weaker in the environment of E<sub>1</sub>. Further, if the acid-base equilibrium shifts and one GLU loses a proton, the change in Coulombic interaction energy can be calculated with

$$dE_{Coul}(r) = \sum_{i} \frac{|q_i||q|}{4\pi\epsilon_0 r_i^2} \times e^{-r_i k(r)} \propto e^{-r_i \lambda_D(r)^{-1}}$$
(12)

Where k(r) is the inverse of Debye length,  $r_i$  is the distance between the new charge and every other charge. Therefore, the energy penalty is exponentially higher if the charge is buried deeper inside the fiber. The synergistic effect of low permittivity and low ion concentration suggests that  $E_1$  is protonated.

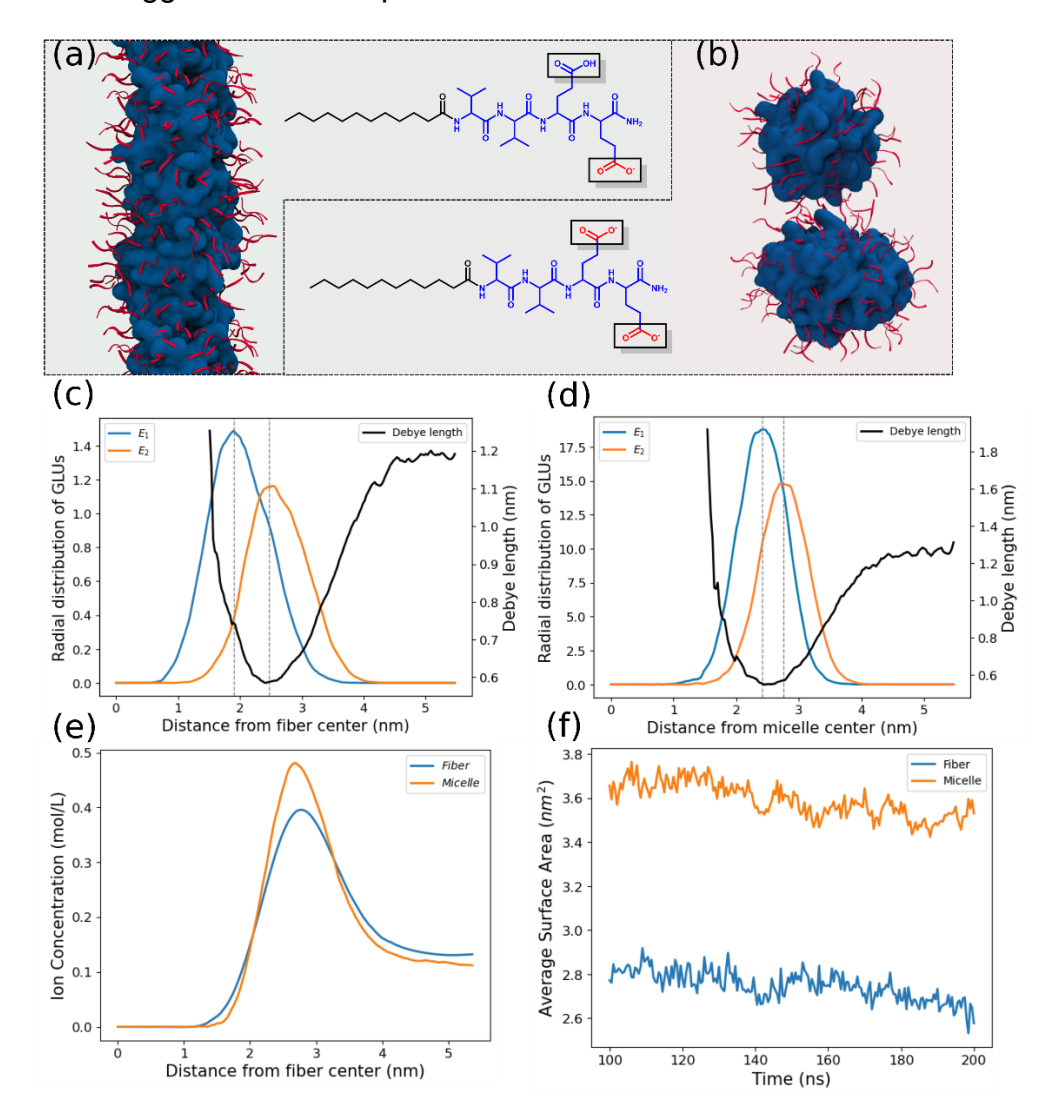
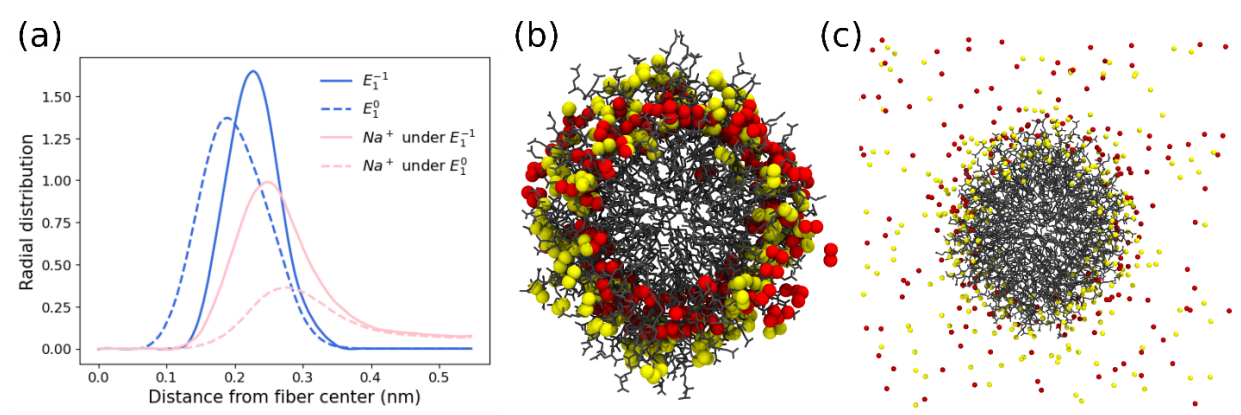


Figure 2. Atomistic simulations results of the peptide amphiphiles. (a) The equilibrium snapshot of the  $C_{12} - VVE_1^0E_2^{-1}$  fiber. A densely packed fiber is formed. (b) The equilibrium snapshot of the  $C_{12} - VVE_1^{-1}E_2^{-1}$  system. The fiber breaks down into 2 micelles. Blue surfaces are the  $C_{12}$  hydrophobic cores and the red cartoons are the amino acids. The GLUs RDFs and the Debye length as a function of distance from the  $C_{12}$  center of (c) the fiber and (d) the micelles. Both  $E_2$  have lower and wider peaks relative to  $E_1$  because further away from the center, the GLUs have more free space. The Debye length near the hydrophobic cores is huge due to the sparse distribution of ions. It drops drastically as the distance from the center increases and reaches the minimum around the margin of the fiber/micelle due to the ion condensations. (e) The Ion condensation around the fiber and the micelle. The micelle has more ion condensed around it. (f) The average solvent-accessible surface area per PA molecule. The micelle has a much larger average surface area, allowing more ions and solvent molecules to diffuse into the micelle.

A similar analysis is performed on the micelles where both GLUs are charged in the PA molecules. The RDF of E<sub>1</sub>, E<sub>2</sub>, and Debye length are shown in *Fig. 2d*. The local Debye length at E<sub>1</sub> ( $\lambda_3 = 0.55 \ nm$ ) and at E<sub>2</sub> ( $\lambda_4 = 0.56 \ nm$ ) of micelles has very close values and is less than the Debye length near the cylindrical fiber (~35.7% less than  $\lambda_1$  and ~8.9% less than  $\lambda_2$ ). Both GLUs in the micelle experience significantly stronger electrostatic screening. Compared with cylindrical fibers, micelles have larger unit surface areas (~31%) (*Fig. 2f*). Sparse distribution of the GLUs mitigates the Coulombic repulsion. Furthermore, the micelles occupy less volume fraction at the same distance r from the center, compared with fibers. More free space allows more solvent molecules and ions to diffuse into the micelles, increasing the ion condensation around the micelle hydrophobic cores (*Fig. 2e*).

To further prove the statement that limited access to water and ions prevents deprotonation of the carboxylic groups, an artificial structure of fiber with -2e charges in each PA molecule is simulated by fixing the terminal atom of C<sub>12</sub> with a position restraining force. The results are shown in *Fig. 3.* The RDF of the E<sub>1</sub> group has a shift away from the fiber center as well as a narrower peak. The RDF suggests more extended PA chains in the artificial structure. A less compact structure is generated. Meanwhile, the distribution of Na<sup>+</sup> shifts toward the center of the fiber, indicating Na<sup>+</sup> penetrates deeper into the fiber. The narrowing gap between two distribution function peaks indicates E<sub>1</sub> has more access to ions and therefore screens out the electrostatic repulsions and gains electrostatic attraction energies via binding due to the smaller local permittivity. However, internally the fiber is dehydrated, increasing the local electrostatic potential. It is entropically unfavorable for free Na<sup>+</sup> to move from a polar medium to a less polar medium and to bind with the fiber. Therefore, the synergy of these effects generates potential destructive effects on the cylindrical fiber structure.



**Figure 3**. Simulation results of artificial supramolecular nanofiber structure. (a) The RDF of E<sub>1</sub> and Na<sup>+</sup>. E<sub>1</sub> has more access to Na<sup>+</sup> after deprotonation. The distribution of (b) E<sub>1</sub>, (c) Na<sup>+</sup>. Red stands for the results of single-charged PA (E<sub>1</sub> is uncharged) while yellow stands for the results of double-charged PA (E<sub>1</sub> is charged).

MARTINI 3 coarse-grained simulations produce the expected results (*Fig. 4*). With fully deprotonated C<sub>12</sub>-VVEE PA molecules, only micelles are formed. Two micelles have 64 and 86 PA molecules respectively, qualitatively consistent with atomistic simulations. On the contrary, half-protonated C<sub>12</sub>-VVEE PA molecules form micelles and quickly merge into cylindrical fibers.

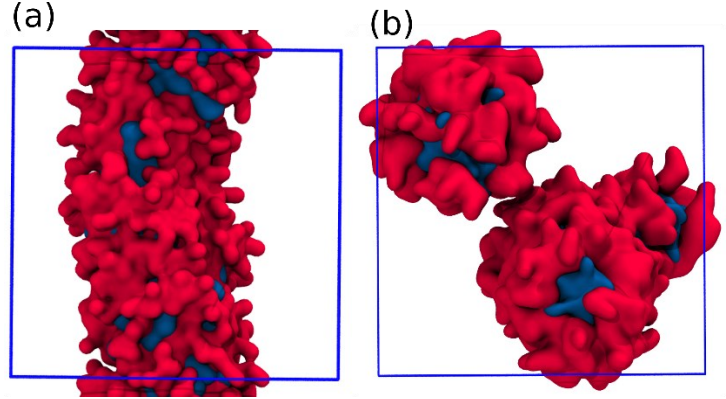


*Figure 4*. The MARTINI3 coarse-grained simulations. (a) the equilibrium snapshot of the  $C_{12} - VVE_1^0E_2$  fiber. A densely packed fiber is formed. (b) The equilibrium snapshot of the  $C_{12} - VVE_1^{-1}E_2$  system. Two micelles form, consistent with the atomistic simulation results.

To obtain the experimental pKa values of the GLUs in the PA molecules, titration on the C<sub>12</sub>-VVEE is carried out. We also write the pH of the solution as an analytical function of the added volume of NaOH based on the acid-base equilibrium, with 2 distinct pKas as fitting parameters (details are included in the SI). The titration curve and fitting curve are given in *Fig. 5a*, and the pKa values are given in *Table 1*. A large shift in the pKas is observed. Under the fiber self-assembly experiments (pH =  $7.3 \sim 7.4$ ), the protonation states are calculated with Henderson–Hasselbalch equation<sup>37</sup>:

$$\alpha = \frac{1}{1 + 10^{pH - pKa}}$$

where  $\alpha$  is the percentage of the acidic form (charge-neutral) of the GLU residue under a certain pH. Only 4% of the inner GLUs (E<sub>1</sub>) are charged while almost all the outer GLUs (E<sub>2</sub>) are negatively charged. The result is consistent with our hypothesis and simulation results.

	Theoretic pKa	Experimental pKa	ΔpKa	Charged %
$E_1$	4.1	9.3	5.2	4%
E2		6.0	1.9	99%

*Table 1*. The pKa of GLUs from titrations.

It became necessary to validate experimentally if there is indeed a morphological transition in the self-assembled structures formed by C<sub>12</sub>-VVEE when the solution pH is changed from 7 to 10. Dynamic light scattering (DLS) is first used to probe the size changes. Given the difficulty of accurately fitting the filamentous nanostructures with a mathematic model, we use the correlation functions to qualitatively assess their size differences. These correlation functions can be calculated from the time-dependent intensity trace using the equation:

$$G(\tau) = \int_0^\infty I(t) \, I|(t+\tau)dt$$

As can be seen from *Fig. 5b*, solutions at both pH 7 and pH 10 show evidence of forming self-assembled structures. At pH 10, the curve is steeper and decays more rapidly at a much shorter timescale than that at pH 7, implying the formation of smaller particles of less polydispersity. These data corroborate our simulation results, which suggest that at pH 10, C<sub>12</sub>-VVEE forms filamentous nanostructures at pH 7 but spherical particles at pH 10.

The structural transition from filamentous nanostructures at pH 7 to discrete particles at pH 10 was further validated using transmission electron microscopy (TEM) imaging. *Fig. 5c, 5d* reveals clearly that  $C_{12}$ -VVEE assembles into filaments at pH 7, but discrete particles of varying sizes (diameter:  $18.9 \pm 9.6$  nm) at pH 10. The irregularity in particle shapes may be attributed to a drying effect during the TEM sample preparation and staining process in which the peptide amphiphile concentration and solution pH were likely varied. Nevertheless, a clear morphological transition in the assembled  $C_{12}$ -VVEE structure is observed as the pH was raised from 7 to 10. The experimental results are highly consistent with theoretical predictions.

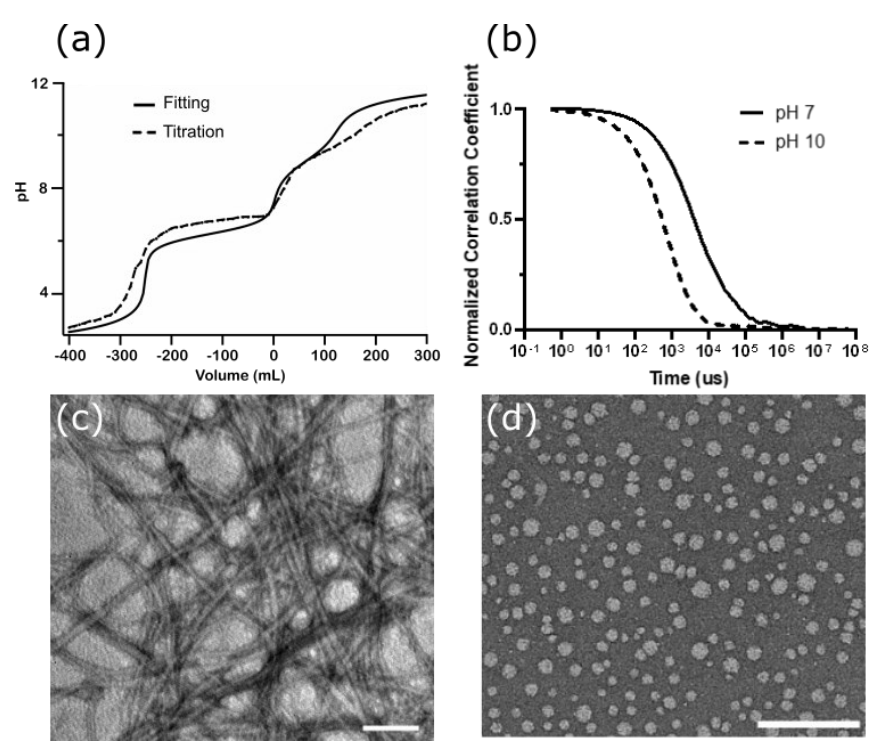


*Figure 5*. (a) Titration and fitting curves of C<sub>12</sub>-VVEE. (b) Normalized correlation coefficient functions for solutions of 100 mM C<sub>12</sub>-VVEE assembled at pH 7 and pH 10 at 25.0 °C. Representative transmission electron microscopy (TEM) images of supramolecular nanostructures formed by C<sub>12</sub>-VVEE at (c) pH 7 and (d) pH 10. Prior to imaging, TEM samples were negatively stained using an aqueous solution of 2 wt% uranyl acetate. Scale bars indicate 200 nm.

To determine the possibility of micellization in PA with longer hydrocarbon tails, another PA fiber consisting of C<sub>16</sub>-VVEE is modeled and simulated (*Fig. 6a*) with different charge states. Similarly, in one system, both Glus in the PA are fully charged while in the other system, only E<sub>2</sub> is charged. Compared with C<sub>12</sub>-VVEE systems, both C<sub>16</sub>-VVEE systems form fibers. The hydrophobicity is stronger in the C<sub>16</sub>-VVEE systems, which compensates for the electrostatic penalties even when both GLUs are charged. Similar to results from the artificial C<sub>12</sub> fiber, the ions concentrate more and diffuse deeper into the fiber when the nanofiber carries 2 negative charges (*Fig. 6b*). During the equilibration, the doubly charged fiber quickly expands in the z direction to decrease the linear charge density (Fig. 6c). On the contrary, the single charged fiber further condenses during the equilibration. The linear density of the half-protonated fiber (20.86 PA/nm) is 59% larger than the fully charged fiber (13.1 PA/nm) while the radius of the half-protonated fiber is only slightly larger than the fully charged fiber. The half-protonated fiber has less extended PA chains and hence a much more compact structure. The simulations further demonstrate that regardless of the assumptions on the charge states of PA molecules, MD simulations produce qualitatively similar results. However, significant quantitative inconsistencies are observed. Moreover, here, we simulated the physical properties of the fibers without the presence of other molecules. Large differences in molecular binding should be expected when other molecules are included.

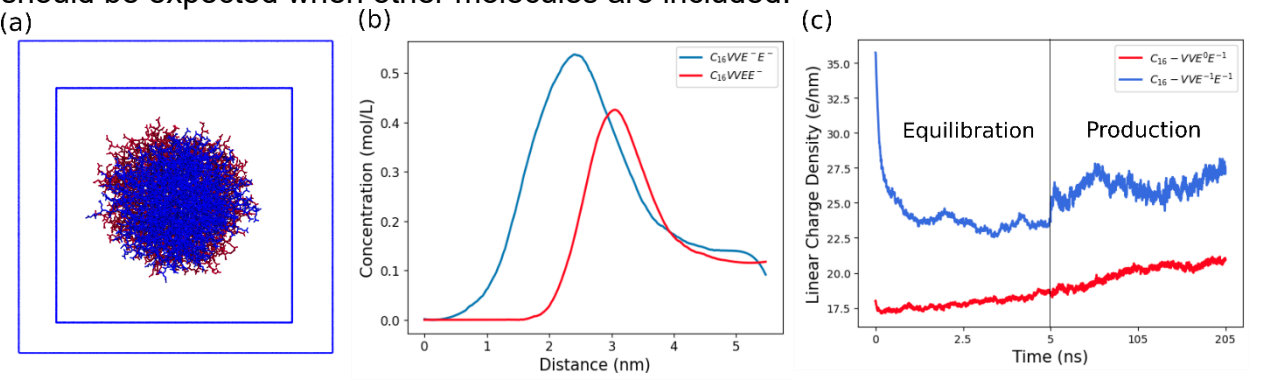


**Figure 6**. All-atom simulations for  $C_{16}VVEE$  fibers. (a) the final snapshot of the  $C_{16}-VVE_1E_2$  fibers. The red surface is the half-protonated fiber, the blue surface is the fully charged fiber, and the blue squares are the simulation boxes. Two snapshots overlap to show the relative size of the fibers. (b) The ion condensation of the two systems. The peak of ion concentrations in the fully charged fiber system is much higher, indicating a stronger ion condensation. (c) The linear charge density of fibers. The double-charged fiber quickly expands to reduce charge density.

The oversimplified model with all amino acids charged does not construct a stable cylindrical fiber in the C<sub>12</sub>-VVEE system because of the short hydrophobic chain and weaker hydrophobic interactions compared with other simulation work<sup>48–50</sup> on PA superstructure systems. Notably, for other PA systems, the all-charged model may generate desired superstructures despite the inaccurate assumption but does not give accurate descriptions of physical properties. Extra caution is required if the all-charged model is used to study systems involving complex interactions such as molecular binding and phase separation. Overestimation of the charge density could lead to distinct ion distributions and electrostatic potentials over superstructures' surfaces. Therefore, the oversimplified model possibly introduces challenges in calculating effective charges and predicting interactions involving PA superstructures. Careful examination and validation should be performed to determine the actual charge states of PAs in superstructures.

# **Conclusions**

In this paper, we report the acid-base equilibrium that exists in the PA self-assembly systems. Both atomistic and coarse-grained Simulations on two  $C_{12}$ -VVEE fiber systems with different protonation states of GLUs yield two different final structures. The PAs with **-2e** charges generate micelles while PAs with **-1e** charges form densely packed fibers that corroborated well with our experimental observations. Analysis reveals that the microenvironments of  $E_1$  yield a low relative permittivity, limited access for counter ions, and a condensed distribution of GLUs. The synergistic effects further boost the Coulombic repulsion between the negative charges and prevent the inner GLU from deprotonation in nanofibers. A titration study was performed, confirming the existence of distinct pKa values for the two neighboring glutamic acid residues. Simulations of  $C_{16}$ -VVEE fibers further demonstrate that MD simulations may yield similar results even with

different assumptions of amino acids' protonation states. However, the physical properties of the fibers formed under the assumptions are significantly different. The results indicate all-charged models might be oversimplified and inaccurate. That is, as found in previous studies of peptide assembly including continuum<sup>32</sup>, coarse grained<sup>35</sup> and/or all atom models<sup>48</sup>, our results indicate that acid-base equilibrium should be considered in modeling PA supramolecular assembly systems.

# **Supporting Information**

Peptide amphiphile synthesis and characterization; Peptide amphiphile self-assembly, titration, and characterization; Fitting of the titration curve; Atomistic Simulations details; Coarsegrained Simulations details; RP-HPLC chromatogram and MALDI-TOF mass spectra.

# **Acknowledgment**

This work is supported by The National Science Foundation under Award Number 2119686.

# Reference

- (1) Dasgupta, A.; Das, D. Designer Peptide Amphiphiles: Self-Assembly to Applications. *Langmuir* 2019, 35 (33), 10704–10724. https://doi.org/10.1021/ACS.LANGMUIR.9B01837
- (2) Qi, R.; Zhang, P.; Liu, J.; Zhou, L.; Zhou, C.; Zhang, N.; Han, Y.; Wang, S.; Wang, Y. Peptide Amphiphiles with Distinct Supramolecular Nanostructures for Controlled Antibacterial Activities. *ACS Appl. Bio Mater.* **2018**, *1* (1), 21–26. https://doi.org/10.1021/ACSABM.8B00005
- (3) Chen, C.; Chen, Y.; Yang, C.; Zeng, P.; Xu, H.; Pan, F.; Lu, J. R. High Selective Performance of Designed Antibacterial and Anticancer Peptide Amphiphiles. *ACS Appl. Mater. Interfaces* **2015**, *7* (31), 17346–17355. https://doi.org/10.1021/ACSAMI.5B04547
- (4) Hartgerink, J. D.; Beniash, E.; Stupp, S. I. Self-Assembly and Mineralization of Peptide-Amphiphile Nanofibers. *Science* **2001**, *294* (5547), 1684–1688. https://doi.org/10.1126/SCIENCE.1063187
- (5) Palmer, L. C.; Newcomb, C. J.; Kaltz, S. R.; Spoerke, E. D.; Stupp, S. I. Biomimetic Systems for Hydroxyapatite Mineralization Inspired by Bone and Enamel. *Chem. Rev.* **2008**, *108* (11), 4754–4783. https://doi.org/10.1021/CR8004422
- (6) Li, L.-L.; Qi, G.-B.; Yu, F.; Liu, S.-J.; Wang, H.; Li, L.; Liu, S.; Qi, G.; Wang, H.; Yu, F. An Adaptive Biointerface from Self-Assembled Functional Peptides for Tissue Engineering. *Adv. Mater.* **2015**, *27* (20), 3181–3188. https://doi.org/10.1002/ADMA.201500658.
- (7) Kumar, D.; Workman, V. L.; O'Brien, M.; McLaren, J.; White, L.; Ragunath, K.; Rose, F.; Saiani, A.; Gough, J. E. Peptide Hydrogels—A Tissue Engineering Strategy for the Prevention of Oesophageal Strictures. *Adv. Funct. Mater.* **2017**, 27 (38), 1702424. https://doi.org/10.1002/ADFM.201702424.
- (8) Preslar, A. T.; Tantakitti, F.; Park, K.; Zhang, S.; Stupp, S. I.; Meade, T. J. 19F Magnetic Resonance Imaging Signals from Peptide Amphiphile Nanostructures Are Strongly Affected by Their Shape. *ACS Nano* **2016**, *10* (8), 7376–7384. https://doi.org/10.1021/ACSNANO.6B00267
- (9) Bull, S. R.; Guler, M. O.; Bras, R. E.; Venkatasubramanian, P. N.; Stupp, S. I.; Meade, T. J. Magnetic Resonance Imaging of Self-Assembled Biomaterial Scaffolds. *Bioconjug. Chem.* 2005, 16 (6), 1343–1348. https://doi.org/10.1021/BC050153H
- (10) Sai, H.; Lau, G. C.; Dannenhoffer, A. J.; Chin, S. M.; Dorddević, L.; Dorddević, L.; Stupp, S. I.; Imaging Supramolecular Morphogenesis with Confocal Laser

- Scanning Microscopy at Elevated Temperatures. *Nano Lett.* **2020**, *20* (6), 4234–4241. https://doi.org/10.1021/ACS.NANOLETT.0C00662
- (11) Peters, E. B.; Karver, M. R.; Sun, K.; Gillis, D. C.; Biswas, S.; Clemons, T. D.; He, W.; Tsihlis, N. D.; Stupp, S. I.; Kibbe, M. R. Self-Assembled Peptide Amphiphile Nanofibers for Controlled Therapeutic Delivery to the Atherosclerotic Niche. *Adv. Ther.* **2021**, *4* (9), 2100103. https://doi.org/10.1002/ADTP.202100103.
- (12) Martin, S.; Harrington, D. A.; Ohlander, S.; Stupp, S. I.; McVary, K. T.; Podlasek, C. A. Peptide Amphiphile Nanofiber Hydrogel Delivery of Sonic Hedgehog Protein to the Penis and Cavernous Nerve Suppresses Intrinsic and Extrinsic Apoptotic Signaling Mechanisms, Which Are an Underlying Cause of Erectile Dysfunction. Nanomedicine Nanotechnology, Biol. Med. 2021, 37. https://doi.org/10.1016/J.NANO.2021.102444.
- (13) Barrett, J. C.; Tirrell, M. V. Peptide Amphiphile Micelles for Vaccine Delivery. Methods Mol. Biol. 2018, 1798, 277–292. https://doi.org/10.1007/978-1-4939-7893-9 21
- (14) Singha, N.; Gupta, P.; Pramanik, B.; Ahmed, S.; Dasgupta, A.; Ukil, A.; Das, D. Hydrogelation of a Naphthalene Diimide Appended Peptide Amphiphile and Its Application in Cell Imaging and Intracellular PH Sensing. *Biomacromolecules* 2017, 18 (11), 3630–3641. https://doi.org/10.1021/ACS.BIOMAC.7B01048
- (15) Li, N.; Li, N.; Yi, Q.; Luo, K.; Guo, C.; Pan, D.; Gu, Z. Amphiphilic Peptide Dendritic Copolymer-Doxorubicin Nanoscale Conjugate Self-Assembled to Enzyme-Responsive Anti-Cancer Agent. *Biomaterials* **2014**, *35* (35), 9529–9545. https://doi.org/10.1016/J.BIOMATERIALS.2014.07.059.
- (16) Ehm, T.; Shinar, H.; Jacoby, G.; Meir, S.; Koren, G.; Segal Asher, M.; Korpanty, J.; Amir, R. J.; Rädler, J. O.; Beck, R. Self-Assembly of Tunable Intrinsically Disordered Peptide Amphiphiles. *Biomacromolecules* **2023**, *24* (1), 98–108. https://doi.org/10.1021/ACS.BIOMAC.2C00866
- (17) Barrett, J. C.; Ulery, B. D.; Trent, A.; Liang, S.; David, N. A.; Tirrell, M. V. Modular Peptide Amphiphile Micelles Improving an Antibody-Mediated Immune Response to Group A Streptococcus. *ACS Biomater. Sci. Eng.* **2017**, 3 (2), 144–152. https://doi.org/10.1021/acsbiomaterials.6b00422.
- (18) Li, Y.; Lock, L. L.; Wang, Y.; Ou, S. H.; Stern, D.; Schön, A.; Xu, X.; Ghose, S.; Li, Z. J.; Cui, H.; *et al.* Bioinspired Supramolecular Engineering of Self-Assembling Immunofibers for High Affinity Binding of Immunoglobulin G. *Biomaterials* **2018**, 178, 448–457. https://doi.org/10.1016/J.BIOMATERIALS.2018.04.032.
- (19) Li, Y.; Lock, L. L.; Mills, J.; Ou, B. S.; Morrow, M.; Stern, D.; Xu, X.; Ghose, S.; Li, Z. J.; Cui, H.; *et al.* Selective Capture and Recovery of Monoclonal Antibodies by Self-Assembling Supramolecular Polymers of High Affinity for Protein Binding. *Nano Lett.* **2020**, *20* (10), 6957–6965.

- https://doi.org/10.1021/ACS.NANOLETT.0C01297/
- (20) Wang, J.; Liu, K.; Xing, R.; Yan, X. Peptide Self-Assembly: Thermodynamics and Kinetics. *Chem. Soc. Rev.* **2016**, *45* (20), 5589–5604. https://doi.org/10.1039/C6CS00176A.
- (21) Tagliazucchi, M.; Olvera de la Cruz, M.; Szleifer, I. Self-Organization of Grafted Polyelectrolyte Layers via the Coupling of Chemical Equilibrium and Physical Interactions. *Proc. Natl. Acad. Sci.* **2010**, *107* (12), 5300–5305. https://doi.org/10.1073/PNAS.0913340107
- (22) Prusty, D.; Nap, R. J.; Szleifer, I.; Olvera de la Cruz, M. Charge Regulation Mechanism in End-Tethered Weak Polyampholytes. *Soft Matter* **2020**, *16* (38), 8832–8847. https://doi.org/10.1039/D0SM01323D.
- (23) Hudson, M. H.; Dolzhnikov, D. S.; Filatov, A. S.; Janke, E. M.; Jang, J.; Lee, B.; Sun, C.; Talapin, D. V. New Forms of CdSe: Molecular Wires, Gels, and Ordered Mesoporous Assemblies. J. Am. Chem. Soc. 2017, 139 (9), 3368–3377. https://doi.org/10.1021/JACS.6B10077
- (24) Kamysbayev, V.; James, N. M.; Filatov, A. S.; Srivastava, V.; Anasori, B.; Jaeger, H. M.; Gogotsi, Y.; Talapin, D. V. Colloidal Gelation in Liquid Metals Enables Functional Nanocomposites of 2D Metal Carbides (MXenes) and Lightweight Metals. ACS Nano 2019, 13 (11), 12415–12424. https://doi.org/10.1021/ACSNANO.9B06207
- (25) Bian, T.; Gardin, A.; Gemen, J.; Houben, L.; Perego, C.; Lee, B.; Elad, N.; Chu, Z.; Pavan, G. M.; Klajn, R. Electrostatic Co-Assembly of Nanoparticles with Oppositely Charged Small Molecules into Static and Dynamic Superstructures. *Nat. Chem.* 2021 1310 2021, 13 (10), 940–949. https://doi.org/10.1038/s41557-021-00752-9.
- (26) Faul, C. F. J.; Antonietti, M. Ionic Self-Assembly: Facile Synthesis of Supramolecular Materials. Adv. Mater. 2003, 15 (9), 673–683. https://doi.org/10.1002/ADMA.200300379.
- (27) Gale, P.; Gunnlaugsson, T.; Rehm, T. H.; Schmuck, C. Ion-Pair Induced Self-Assembly in Aqueous Solvents. *Chem. Soc. Rev.* 2010, 39 (10), 3597–3611. https://doi.org/10.1039/B926223G.
- (28) Isom, D. G.; Castañeda, C. A.; Cannon, B. R.; Velu, P. D.; García-Moreno E, B. Charges in the Hydrophobic Interior of Proteins. *Proc. Natl. Acad. Sci.* **2010**, *107* (37), 16096–16100. https://doi.org/10.1073/PNAS.1004213107
- (29) Tang, C.; Smith, A. M.; Collins, R. F.; Ulijn, R. V.; Saiani, A. Fmoc-Diphenylalanine Self-ASsembly Mechanism Induces Apparent PK a Shifts. *Langmuir* **2009**, *25* (16), 9447–9453. https://doi.org/10.1021/LA900653Q

- (30) Behanna, H. A.; Donners, J. J. J. M.; Gordon, A. C.; Stupp, S. I. Coassembly of Amphiphiles with Opposite Peptide Polarities into Nanofibers. *J. Am. Chem. Soc.* **2005**, *127* (4), 1193–1200. https://doi.org/10.1021/JA044863U
- (31) Zaldivar, G.; Vemulapalli, S.; Udumula, V.; Conda-Sheridan, M.; Tagliazucchi, M. Self-Assembled Nanostructures of Peptide Amphiphiles: Charge Regulation by Size Regulation. *J. Phys. Chem. C* **2019**, *123* (28), 17606–17615. https://doi.org/10.1021/ACS.JPCC.9B04280
- (32) Nap, R. J.; Qiao, B.; Palmer, L. C.; Stupp, S. I.; Olvera de la Cruz, M.; Szleifer, I. Acid-Base Equilibrium and Dielectric Environment Regulate Charge in Supramolecular Nanofibers. *Front. Chem.* **2022**, *10*, 145. https://doi.org/10.3389/FCHEM.2022.852164
- (33) Choi, S.; Knoerdel, A. R.; Sing, C. E.; Keating, C. D. Effect of Polypeptide Complex Coacervate Microenvironment on Protonation of a Guest Molecule. *J. Phys. Chem. B* **2023**, 3 (2), 144-152. https://doi.org/10.1021/ACS.JPCB.3C02098/
- (34) Yu, Z.; Erbas, A.; Tantakitti, F.; Palmer, L. C.; Jackman, J. A.; Olvera de la Cruz, M.; Cho, N. J.; Stupp, S. I. Co-Assembly of Peptide Amphiphiles and Lipids into Supramolecular Nanostructures Driven by Anion-π Interactions. *J. Am. Chem. Soc.* **2017**, *139* (23), 7823–7830. https://doi.org/10.1021/JACS.7B02058
- (35) Leung, C.-Y.; Palmer, L. C.; Qiao, B. F.; Kewalramani, S.; Sknepnek, R.; Newcomb, C. J.; Vernizzi, G.; Stupp, S. I.; Bedzyk, M. J.; Olvera de la Cruz, M.; *et al.* Molecular Crystallization Controlled by PH Regulates Mesoscopic Membrane Morphology. *ACS Nano* **2012**, *6* (12), 10901–10909. https://doi.org/10.1021/nn304321w.
- (36) Longo, G. S.; Olvera de la Cruz, M.; Szleifer, I. Molecular Theory of Weak Polyelectrolyte Gels: The Role of PH and Salt Concentration. *Macromolecules* **2011**, 44 (1), 147-158. https://doi.org/10.1021/ma102312y.
- (37) McCourt, J. M.; Kewalramani, S.; Gao, C.; Roth, E. W.; Weigand, S. J.; Olvera de la Cruz, M.; Bedzyk, M. J. Electrostatic Control of Shape Selection and Nanoscale Structure in Chiral Molecular Assemblies. ACS Cent. Sci. 2022, 8 (8), 1169–1181. https://doi.org/10.1021/ACSCENTSCI.2C00447
- (38) Abraham, M. J.; Murtola, T.; Schulz, R.; Páll, S.; Smith, J. C.; Hess, B.; Lindah, E. GROMACS: High Performance Molecular Simulations through Multi-Level Parallelism from Laptops to Supercomputers. *SoftwareX* **2015**, *1*–2, 19–25. https://doi.org/10.1016/J.SOFTX.2015.06.001.
- (39) Huang, J.; Rauscher, S.; Nawrocki, G.; Ran, T.; Feig, M.; De Groot, B. L.; Grubmüller, H.; MacKerell, A. D. CHARMM36m: An Improved Force Field for Folded and Intrinsically Disordered Proteins. *Nat. Methods* **2016**, *14* (1), 71–73. https://doi.org/10.1038/nmeth.4067.

- (40) Miyamoto, S.; Kollman, P. A. Settle: An Analytical Version of the SHAKE and RATTLE Algorithm for Rigid Water Models. *J. Comput. Chem.* **1992**, *13* (8), 952–962. https://doi.org/10.1002/JCC.540130805.
- (41) Humphrey, W.; Dalke, A.; Schulten, K. VMD: Visual Molecular Dynamics. *J. Mol. Graph.* **1996**, *14* (1), 33–38. https://doi.org/10.1016/0263-7855(96)00018-5.
- (42) Michaud-Agrawal, N.; Denning, E. J.; Woolf, T. B.; Beckstein, O. MDAnalysis: A Toolkit for the Analysis of Molecular Dynamics Simulations. *J. Comput. Chem.* 2011, 32, 2319–2327. https://doi.org/10.1002/jcc.21787.
- (43) Hanwell, M. D.; Curtis, D. E.; Lonie, D. C.; Vandermeerschd, T.; Zurek, E.; Hutchison, G. R. Avogadro: An Advanced Semantic Chemical Editor, Visualization, and Analysis Platform. *J. Cheminform.* **2012**, *4* (8), 1–17. https://doi.org/10.1186/1758-2946-4-17
- (44) Martinez, L.; Andrade, R.; Birgin, E. G.; Martínez, J. M. PACKMOL: A Package for Building Initial Configurations for Molecular Dynamics Simulations. *J. Comput. Chem.* **2009**, *30* (13), 2157–2164. https://doi.org/10.1002/JCC.21224.
- (45) Lee, O. S.; Stupp, S. I.; Schatz, G. C. Atomistic Molecular Dynamics Simulations of Peptide Amphiphile Self-Assembly into Cylindrical Nanofibers. *J. Am. Chem. Soc.* **2011**, *133* (10), 3677–3683. https://doi.org/10.1021/JA110966Y
- (46) Souza, P. C. T.; Alessandri, R.; Barnoud, J.; Thallmair, S.; Faustino, I.; Grünewald, F.; Patmanidis, I.; Abdizadeh, H.; Bruininks, B. M. H.; Marrink, S. J.; et al. Martini 3: A General Purpose Force Field for Coarse-Grained Molecular Dynamics. Nat. Methods 2021, 18 (4), 382–388. https://doi.org/10.1038/s41592-021-01098-3.
- (47) Gaddam, P.; Ducker, W. Electrostatic Screening Length in Concentrated Salt Solutions. *Langmuir* **2019**, *35* (17), 5719–5727. https://doi.org/10.1021/ACS.LANGMUIR.9B00375
- (48) Cote, Y.; Fu, I. W.; Dobson, E. T.; Goldberger, J. E.; Nguyen, H. D.; Shen, J. K. Mechanism of the PH-Controlled Self-Assembly of Nanofibers from Peptide Amphiphiles. *J. Phys. Chem. C* 2014, 118 (29), 16272–16278. https://doi.org/10.1021/JP5048024
- (49) Lee, O.-S.; Cho, V.; Schatz, G. C. Modeling the Self-Assembly of Peptide Amphiphiles into Fibers Using Coarse-Grained Molecular Dynamics. *Nano Lett* **2012**, *12*, 4907–4913. https://doi.org/10.1021/nl302487m.
- (50) Xiong, Q.; Stupp, S. I.; Schatz, G. C. Molecular Insight into the β-Sheet Twist and Related Morphology of Self-Assembled Peptide Amphiphile Ribbons. *J. Phys. Chem. Lett.* **2021**, *12* (46), 11238–11244. https://doi.org/10.1021/ACS.JPCLETT.1C03243